Thin Solid Films 848 (2026) 140992

Contents lists available at ScienceDirect

Thin Solid Films

journal homepage: www.elsevier.com/locate/tsf

$BaZrS_3$ perovskite thin films by H_2S sulfurization of solution-processed precursors

Ibrahim Simsek [a,b,*], Marin Rusu [a], Galina Gurieva [a], Hannes Hempel [a], Adriana Röttger [a], José A. Márquez [a], Thomas Unold [a,*], Susan Schorr [a,c]

[a] Department Structure and Dynamics of Energy Materials, Helmholtz-Zentrum Berlin für Materialien und Energie GmbH, Hahn-Meitner-Platz 1, 14109, Berlin, Germany
[b] Light Technology Institute, Karlsruhe Institute of Technology, Engesserstrasse 13, 76131, Karlsruhe, Germany
[c] Institute of Geological Sciences, Freie Universität Berlin, Malteserstr. 74-100, 12249, Berlin, Germany

ARTICLE INFO

Keywords:
Chalcogenide perovskites
Molecular ink
Solution processing
Thin films
Photoelectron yield spectroscopy

ABSTRACT

Inorganic $BaZrS_3$ perovskite is a potential non-toxic chalcogenide material for photovoltaic applications due to its bandgap tunability, thermodynamic stability and the abundance of constituent elements. This study demonstrates the preparation of $BaZrS_3$ thin films from solution-processed precursors, with which the formation of secondary phases could be avoided. Metal-organic precursors were spin-coated and subsequently sulfurized at various temperatures, ranging from 600 °C to 1100 °C, using Ar-diluted H_2S gas. The atomic ratio of the films, determined by X-ray fluorescence spectroscopy, reveals an equimolar ratio of Ba and Zr both before and after the sulfurization process. No oxide secondary phases are detected in the sulfurized films. The Le Bail analysis of the X-ray diffractograms reveals the formation of $BaZrS_3$ in the orthorhombic perovskite-type crystal structure (space group *Pnma, #62*). We observe an increased crystallinity of the films with increasing preparation temperature, accompanied by a decrease of the bandgap from 2.16 ± 0.04 eV at 900 °C to 2.02 ± 0.01 eV at 1000 °C. For sulfurization temperatures of 1100 °C, a secondary Ruddlesden-Popper phase, $Ba_4Zr_3S_{10}$, is detected. Kelvin probe measurements of the films prepared at 1000 °C indicate *n*-type conductivity with a work function of ~4.26 eV. Photoelectron yield spectroscopy reveals an ionization energy of ~5.38 eV which defines the position of the valence band maximum. The experimental density of state spectra are found in good agreement with the theoretical data. The sum charge carrier mobility of ~2.4 $cm^2V^{-1}s^{-1}$ is determined from optical-pump–terahertz-probe spectroscopy measurements.

1. Introduction

Inorganic chalcogenide perovskite-type materials have gained increasing interest as potentially stable absorbers for application in solar cells owing to their promising optoelectronic properties related to their structure type, in analogy to their hybrid organic-inorganic counterparts which have enabled photovoltaic devices with efficiencies >25% [1,2]. Inorganic perovskites are described by the formula AMX_3 with A denominating a group II cation (e.g., Ba^{2+}, Ca^{2+}, Sr^{2+}), M a group IV transition metal (e.g., Hf^{4+}, Ti^{4+}, Zr^{4+}) and X a chalcogen anion (S^{2-}, Se^{2-}). Density functional theory (DFT) was used to narrow down the range of chalcogenide perovskite compounds of interest for solar cell applications [3–6]. Among these range of perovskites, $BaZrS_3$ is regarded as of a particular interest due to its stability, e.g., of its crystal structure and optical properties after months of storage in air and being repeatedly rinsed with deionized water [4]. Preparation of $BaZrS_3$ thin films have been reported by both, dry and wet processing techniques. Dry approaches typically involve either reactive annealing of sputtered binary sulfide precursors or sulfurization of pre-formed ternary oxide perovskites such as $BaZrO_3$, though both routes frequently produce secondary phases, including ternary oxides [7–10]. Molecular beam epitaxy (MBE) provides an additional dry route, wherein Ba and Zr are co-evaporated in an H_2S ambient to directly form $BaZrS_3$. MBE can deliver near-ideal stoichiometry and excellent compositional control, but its low throughput, limited substrate area, and the need to maintain a narrow sulfur-rich growth window mean it is not generally superior to solution-based methods for scalable processing [11,12]. The wet processing methods were applied for the preparation of $BaZrS_3$ by using

* Corresponding authors at: Department Structure and Dynamics of Energy Materials, Helmholtz-Zentrum Berlin für Materialien und Energie GmbH, 14109, Berlin, Germany.
E-mail addresses: ibrahim.simsek@kit.edu (I. Simsek), unold@helmholtz-berlin.de (T. Unold).

https://doi.org/10.1016/j.tsf.2026.140992
Received 16 January 2026; Received in revised form 18 June 2026; Accepted 22 June 2026
Available online 25 June 2026

solutions from precursors of barium and zirconium [13–15]. Though, as in the case of the dry processing, those thin films contained secondary phases due to formation of oxides, e.g., $BaZrO_3$ during the step prior to sulfurization. However, note that with solution-based processing, molecular inks can be applied with the advantage of easily adjustable compositions and the inclusion of additives [16]. Additionally, an ink recipe can be easily adapted to other materials in the same class. That makes possible an easy upscaling of the developed technology for the deposition of the films on large area substrates.

In this study, we report the synthesis of $BaZrS_3$ perovskite thin films from precursors processed from solution-inks of acetate and iodide mixtures. The developed inks were deposited by spin-coating to form the precursor layers. The as-deposited precursors were subsequently sulfurized in an argon-diluted H_2S ambient at temperatures between 600–1100 °C. The structural and optoelectronic properties of the films were studied finally demonstrating the formation of $BaZrS_3$ perovskite thin films free of secondary phases.

2. Experimental

2.1. Solution preparation route and precursor deposition

Unlike the most-studied halide perovskites, the preparation of chalcogenide perovskites from their sulfide binaries is difficult since the solubilities of metal sulfides are relatively low [17]. Metal acetates, however, are highly soluble in aqueous solutions and react easily with H_2S [17,18]. Yet, the usage of water as a solvent may cause metal hydroxide formations, which turn into metal oxides at higher temperatures and can thus result in oxide secondary phases. To circumvent this, we have chosen the anhydrous dimethylformamide (DMF) as a solvent. Note that DMF is also a polar solvent like water, being commonly used in the solution processing synthesis of halide perovskites. Considering the necessity of the adjustment of the pH of the solution, we additionally used glacial acetic acid to increase the solubility of the binaries in DMF. In addition, acetic acid has been used to prevent the solvolysis by keeping the components in the acetate form, by giving acetate ions to the solution [19]. According to the catalytic studies of sulfurization reactions of chalcogenide perovskites, the addition of halide compounds increases the reaction rate and decreases the reaction duration from days to hours [20,21]. We show that adding a small amount of barium iodide to the solution of the acetate compounds improves the coverage of the material on the applied substrate (see appendix Fig. A1**(a)**). Furthermore, we use barium iodide rather than the iodide compound of zirconium, since we have demonstrated its effective sulfurization as can also be seen in Fig. A2 in appendix**.** By mixing the acetate and the iodide compounds of barium, the solubility of the barium cation is also advanced due to the elimination of the common ion effect.

To prepare the precursor solution, 1.07 mmol of BaI_2 (Santa Cruz Biotechnology, >%98), 3.92 mmol of $Ba(CH_3COO)_2$ (ACROS Organics, 99+%) were dissolved in a mixture of 3 mL of N—-N-dimethylformamide (DMF) (Sigma-Aldrich, 99.9%) with 3 mL of acetic acid (Sigma-Aldrich, >99.8%), and 1.77 mL of $Zr(CH_3COO)_4$ solution (Sigma-Aldrich, 4.07 mmol of Zr in dilute acetic acid). The solution was stirred in an N_2-filled glovebox at room temperature for 30 min. A clear and transparent solution was obtained.

Quartz substrates (1-inch x 1-inch) were cleaned with acetone immediately before being coated with 200 μL of the precursor solution. For measurements requiring a conductive substrate, glassy carbon substrates were coated alongside quartz substrates following the same deposition procedure. The spin-coating processes were conducted via static dispensing in the same glovebox at 1000 rpm for 10 s followed by a ramped up within 3 s to 3500 rpm, and subsequently spun for 20 s. The spin-coated layer was then heated to 250 °C for 2 min. The spin-coating procedure and heating were repeated three times. An additional annealing process at 250 °C for 10 min was performed to ensure the complete evaporation of the residual DMF resulting in the final precursor thin films. We note that for obtaining precursor films with [Ba]/[Zr]=1:1 under those spin-coating conditions, the solution needed to be prepared slightly Ba-rich ([Ba]/[Zr]≈5:4), presumably due to a lower sticking coefficient of Ba on substrates as compared to Zr.

2.2. Sulfurization of thin film precursors

The precursor thin films were placed in a quartz boat and quickly transferred into a tube furnace for sulfurization. The furnace was twice evacuated and flushed with argon (6N purity), and then flushed with 5% H_2S diluted in argon. Before starting the annealing process, the gas inlet was set to 60 sccm of 5% H_2S (± 0.15 Vol %, Air Liquide) in argon. After achieving a constant flow, the furnace was switched on. The desired temperatures between 600 and 1100 °C for each experiment were set to be reached within 30 min. After 30 min of the sulfurization process, the furnace was switched off. The gas flow was changed to pure argon when the temperature reached 400 °C during cooling. The samples were collected when the room temperature was reached.

2.3. Characterization methods

The atomic ratio and thicknesses of the films were determined by X-ray fluorescence (XRF) analysis using a Bruker M4 Tornado with a Rh-tube. The XRF measurements were carried out with a spot size of 20 μm in diameter by using the poly-capillary optic of the instrument.

The crystal structure and phase content of the films was determined from grazing incidence X-ray diffraction (GIXRD) measurements with a PANalytical X'Pert MPD Pro instrument with a Cu Kα radiation source ($\lambda(Cu_{K\alpha1})$=0.154056 nm) at an incidence angle of 1° The step size of the GIXRD measurement was 0.05° and the time per step was 3 s.

Scanning electron microscopy (SEM) images were recorded by a LEO Gemini 1530 apparatus. The instrument is equipped with a conventional and an In-Lens detector for secondary electrons. The imaging was performed at an electron acceleration voltage of 5 kV.

Raman spectra were measured using a Renishaw inVia confocal Raman spectrometer equipped with a Diode-Pumped Solid-State laser with a wavelength / excitation energy of 532 nm / 2.33 eV.

A Perkin Elmer Lambda 1050 spectrometer was used for UV–Vis measurements. Transmittance (T) and reflectance (R) were measured and used for the calculation of the absorptance (A).

Kelvin probe (KP) and photoelectron yield spectroscopy (PYS) were combined to measure the work function (Φ) and ionization energy (E_i) of the prepared thin films, respectively, by employing a KP Technology SKP5050-APS02 setup under inert N_2 atmosphere (5N purity) at ambient pressure. The setup was placed in a Faraday cage to shield external electric fields and enable controlled illumination of the sample. The samples were contacted with carbon tape. The Kelvin probe was a 2.0 mm diameter tip with a gold-alloy coating with a work function, Φ_{tip}, calibrated against a gold reference sample. The work function of the sample, Φ_{sample}, is determined according to $\Phi_{sample} = \Phi_{tip} + e{\cdot}CPD$ where e is the elementary charge and CPD is the contact potential difference between the Kelvin tip and the investigated sample. The CPD was measured with a resolution of 1–3 mV. The measurements of the surface photovoltage (SPV) defined as $SPV = CPD_{light} - CPD_{dark}$ were performed using a continuous wave (cw) laser diode with a wavelength/energy of 532 nm/2.33 eV with a light power density of ≈100 mW/cm^2. PYS measurements were performed by using the same Kelvin tip in the static regime. The sample was illuminated by a deuterium light source coupled with a grating monochromator, providing excitation from 3.4 to 7.6 eV. Measurements were conducted with a step of 1 nm and the photoemission threshold was determined with a resolution of 30 meV. Total density of states (DOS) spectra were obtained as the first derivative of the photoelectron yield with respect to photon energy. Further details on the KP-PYS setup and data evaluation can be found elsewhere [22].

The sum mobility of the photogenerated charge carriers was determined from optical-pump–terahertz-probe (OPTP) measurements [23].

To photogenerate charge carriers, laser pulses with a wavelength of 400 nm, a pulse duration of ~150 fs, a repetition rate of 150 kHz and a photon flux per pulse Φ_{laser} of 3.5×10^{13} cm^{-2} were used. The change in the transmission of a terahertz probe pulse was measured by electro-optical sampling in a 1 mm thick ZnTe crystal and modelled by the thin film approximation method. This approach yields the photoconductivity and sum mobility of excited electrons and holes. The THz probe spot size on the film surface was ≈1 mm, averaging the mobility over this area.

3. Results and discussion

3.1. $BaZrS_3$ thin film appearance and morphology

As a result of sulfurization, the transparent precursor thin-films turned into burgundy color, as can be seen in Fig. 1. SEM images in Fig. 1 show that the crystalline size increases with the sulfurization temperature. At 900 °C the crystallite size is <200 nm, while reaching 200 nm at 950 °C and increasing by almost five times to about 1 μm at 1100 °C.

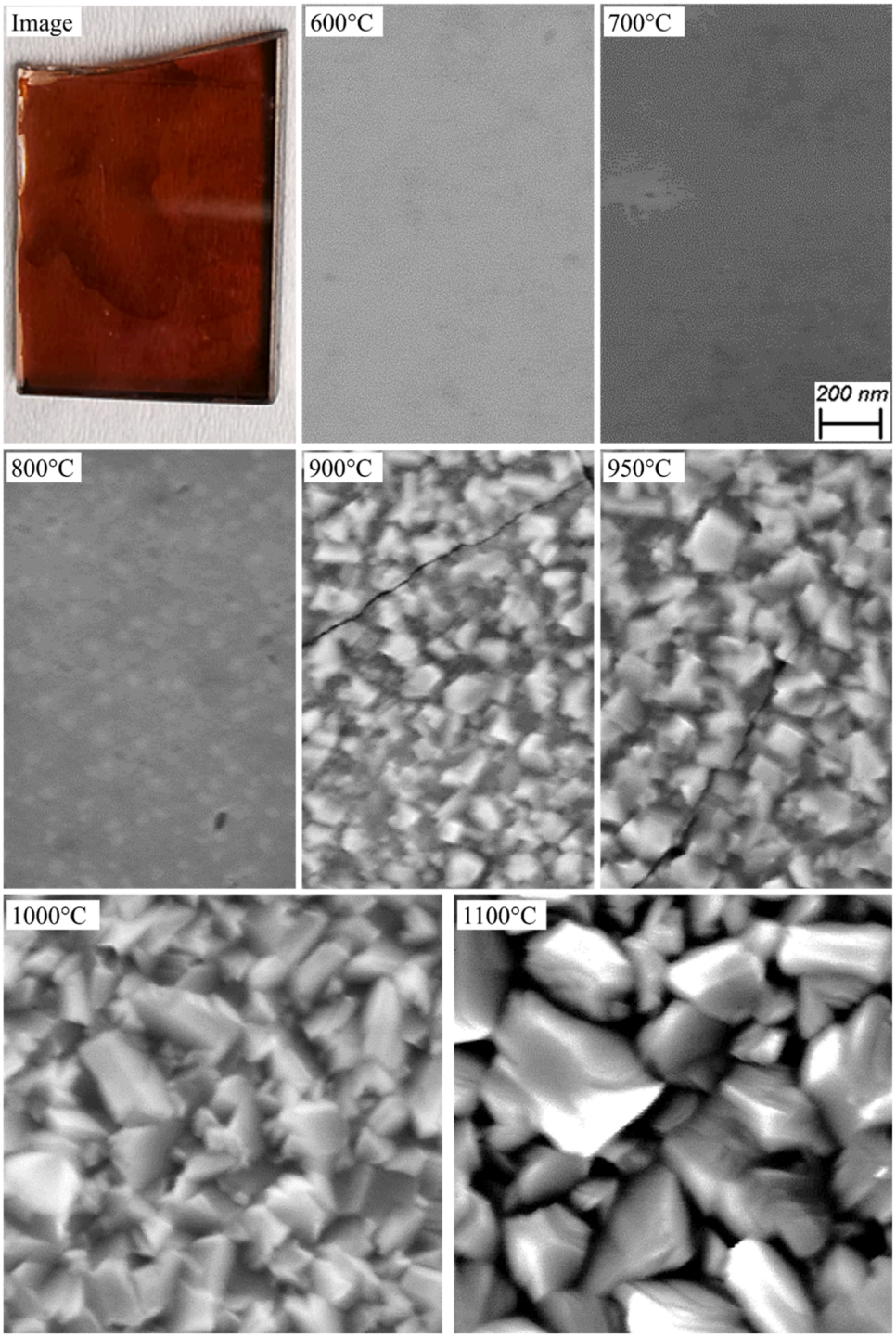

Fig. 1. Photographic image and scanning electron microscopy (SEM) In-Lens images of the $BaZrS_3$ thin films prepared by sulfurization at temperatures from 600 °C to 1100 °C. The scale bar indicated for films sulfurized at 700 °C applies to all the SEM images.

3.2. Atomic ratio and crystal structure of $BaZrS_3$ films

The atomic ratios and thicknesses obtained from XRF measurements on precursors as well as on thin films prepared at annealing temperatures of 800 °C, 900 °C, 950 °C, 1000 °C and 1100 °C are presented in Table 1. Thus, the XRF analysis shows that the sulfurized films achieve an elemental stoichiometry close to the perovskite composition of 1:1:3 at annealing temperatures ≥900 °C. It has been demonstrated that a 1:1:3 atomic ratio is critical for achieving low-oxygen content after sulfurization, even when oxide precursors are employed [24]. The XRF analysis also reveals that the [Ba]/[Zr] atomic ratio does not change significantly after sulfurization, which means that none of these cations are volatile at such temperatures. Note that the volatility of constituent elements can be a major problem for thin films, as it can lead to compositional inconsistencies and defects during deposition, which adversely affects the film's optoelectronic properties, e.g., tin volatility in other related perovskites or kesterites [25]. To estimate the possible oxygen content in the films, we apply the charge neutrality condition [9]. Since the atomic ratio of the films overlap with the perovskite ratio and there is not ion deficiency, it can be concluded that the films prepared at temperatures ≥900 °C do not contain a significant amount of an oxide component.

While the annealing temperature remains high for industrial applications, this study demonstrates that solution-processed precursors can be sulfurized to a high degree. Moreover, samples produced at temperatures below 1000 °C also exhibit considerably high sulfurization rates. It should be noted that the sulfurization time in this study was limited to 30 min; extending the sulfurization duration or increasing the H_2S concentration in the argon atmosphere could potentially improve the sulfurization degree and reduce the defect density in samples processed at lower annealing temperatures in order to reach comparable bandgaps.

The XRD pattern in Fig. 2 shows that up to sulfurization temperatures of 800 °C only very broad peaks are detected denoting the amorphous state of the films. For sulfurization temperatures ≥900 °C prominent Bragg peaks indicating the orthorhombic perovskite crystal structure (space group *Pnma*) of $BaZrS_3$ are observed. No peaks for oxide or sulfide secondary phases are detected. Note that in the case of the $BaZrS_3$ obtained by sulfurization from its ternary oxide, the 110 Bragg peak of $BaZrO_3$ in the cubic perovskite structure (space group $Pm\bar{3}m$) has been reported [9]. At 1100 °C, we observe $BaZrS_3$ along with the trace amounts of $Ba_4Zr_3S_{10}$ from the series of the Ruddlesden-Popper (RP) phases [26–29].

Since the 1000 °C and 1100 °C samples were prepared from the same precursor that was cut into two identical pieces before sulfurization, we can assume that the formation of the RP secondary phase was a result of the increased annealing temperature. Pradhan et al. reported that $BaZrS_3$ is thermodynamically preferable over Ruddlesden-Popper phases, yet RP phases are prone to form under sulfur-poor conditions [30]. Based on this data, we propose that the sulfur source kinetics (sulfur diffusion into the film, preceding sulfide intermediates etc.) changes significantly at 1100 °C, resulting in an essential decrease of the sulfurization rate of $BaZrS_3$.

Table 1
Atomic ratio, thickness and bandgap (E_g) for thin films at various sulfurization temperatures. [Ba]/[Zr] is the cation ratio of the precursor films. [Ba]/[Zr]/[S] indicates the elemental ratio in sulfurized film at the given temperature.

Sulfurization temperature (°C)	Precursor [Ba]/[Zr] (atomic % ± 0.01)	[Ba]/[Zr]/[S] (atomic % ± 0.01)	$BaZrS_3$ film thickness (nm)	E_g[a] (eV)
800	1/0.95	1/0.98/2.06	239 ± 5	-
900	1/1.02	1/1.02/2.81	367 ± 5	2.16 ± 0.04
950	1/1.02	1/1.03/3.00	394 ± 5	2.12 ± 0.11
1000	1/1.02	1/1.03/3.13	394 ± 21	2.02 ± 0.01
1100	1/1.02	1/1.03/2.97	467 ± 46	2.01 ± 0.01

[a] E_g values were calculated from the derivative of the thin film absorptance spectra. The errors stem from standard deviations of the Gaussian peaks to the derivative of absorptance (see appendix).

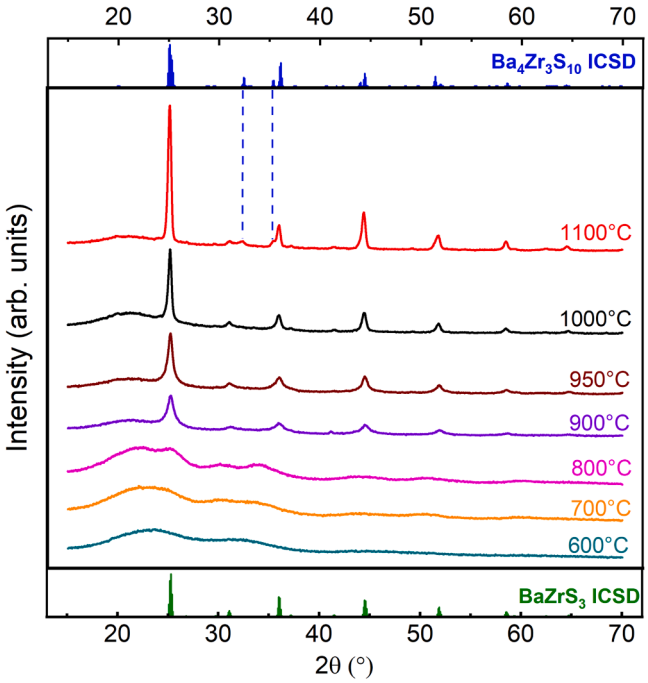

Fig. 2. Grazing incidence diffractograms at incident angle 1° of the $BaZrS_3$ thin films sulfurized at temperatures between 600 °C and 1100 °C. Reference diffractograms are shown from the Inorganic Crystal Structure Database (ICSD) for $BaZrS_3$ (bottom panel, ICSD-23288) and $Ba_4Zr_3S_{10}$ (top panel, ICSD-72656).

The Raman spectra of the $BaZrS_3$ films are shown in Fig. 3. The peak intensities increase with the sulfurization temperature. Most of the peaks in this range evolve from the ZrS_6 octahedra. However, Ba strongly contributes between 100 and 275 cm^{-1} [4]. The modes of the film sulfurized at 1000 °C can be seen in comparison to the publication of Wei et al [8]. For the indexation of the peak modes, the data published by Perera et al. are used as summarized from their theoretical and experimental studies [4]. Raman spectroscopy was also used as a complementary measurement to XRD for the identification of $BaZrS_3$ and its RP phases. Since most of the main XRD peaks are overlapping for these phases, it is difficult to identify them with XRD measurements alone. The vibrational modes of $Ba_4Zr_3S_{10}$ are reported in Kayastha et al. for the peaks at around 340 and 406 cm^{-1} [31].

3.3. Optoelectronic properties

Transmittance (T) and reflectance (R) spectra were measured and absorptance (A) of the films is plotted in Fig. 4**(a)** using the relation $A = 1 - T - R$. The absorptance spectra were then used for the calculation of bandgap values by taking the first derivative (see the derivative plots in appendix, Fig. A6). The obtained E_g data are presented in Fig. 4**(b)**. As it can be seen, the bandgap energies decrease, as the sulfurization temperature increases. However, there is no significant difference between the bandgap energies corresponding to 1000 and 1100 °C. It can be seen in Fig. 4**(b)** that at lower sulfurization temperatures, the absorptances of the samples show higher bandgaps possibly due to the lower crystallinity as concluded from the SEM and XRD data (see also the crystallinity in appendix, Fig. A5).

For further studies of the optoelectronic properties we focus on

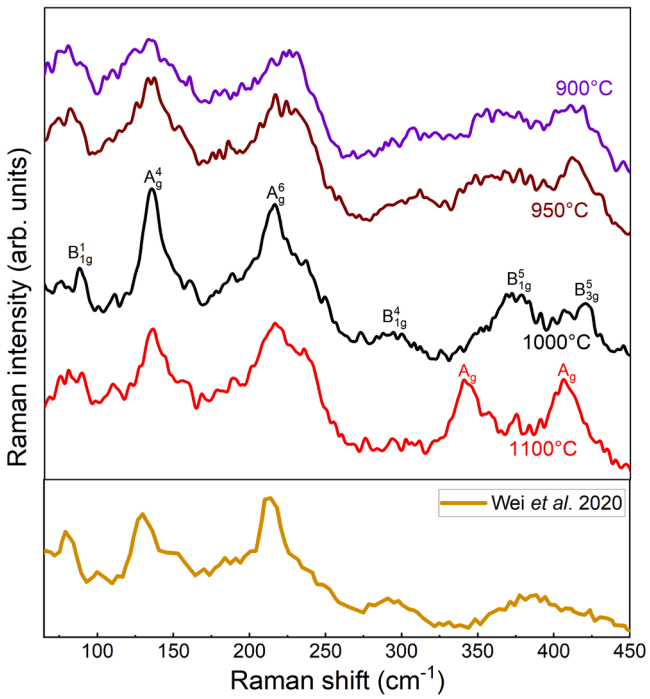

Fig. 3. (top panel) Raman spectra of $BaZrS_3$ measured at the room temperature for the films sulfurized at 900 °C (violet), 950 °C (brown), 1000 °C (black) and 1100 °C (red). (bottom panel) Reference Raman spectrum replotted from Wei *et al.* (2020) for the film sputtered and then annealed at 1050 °C (replotted with permission).

$BaZrS_3$ thin films prepared at 1000 °C with the E_g=2.02 eV since those layers showed the best crystallinity without large amounts of secondary phases (see §3.2). The measured by KP surface work function, Φ, and SPV are presented in Fig. 5**(a)** and **5 (b)**, respectively. The measurements in the dark reveal Φ values and correspondingly Fermi level (E_F) positions at about 4.38 eV, while decreasing under illumination (by a cw laser at an energy of 2.33 eV and light intensity of ≈100 mW/cm^2) to 4.26 eV and 4.31 eV for the $BaZrS_3$ films deposited on quartz glass and glassy carbon substrates, respectively. Note that the samples were only exposed to air for a few minutes during transfer. Consequently, negative SPV values are calculated in Fig. 5**(b)** pointing to an *n*-type conductivity of the films. Lower SPV values recorded for films on glassy carbon indicate an inferior concentration of surface defects. Ionization energy values, E_i, and the corresponding valence band maximum position (E_{VBM}) determined from PYS spectroscopy studies are found to vary between 5.32 eV and 5.38 eV for samples deposited on glassy carbon and quartz glass substrates, respectively. This small difference in E_i may be attributed to slight differences in the thin film's chemical composition. A comparison of our experimental DOS spectra to the theoretically calculated spectra [32] suggests a Zr-poor composition of the layers on glassy carbon. Considering the bandgap of the films, we calculate the electron affinities $EA = E_i$-E_g, which define the respective conduction band minimum (E_{CBM}) positions, at 3.30 eV for films on glassy carbon, and 3.36 eV for layers on quartz glass. We thus find E_F positions relative to E_{CBM} (E_{CBM}-E_F) at 0.90 eV and 1.01 eV for layers on quartz glass and glassy carbon, respectively (see Table 2). Thus, in conjunction with the analysis of the DOS spectra, we conclude that a Zr-poor (Ba-rich) composition may lead to films with a lower concentration of electrons. Note that the value of 0.90 eV for E_{CBM}-E_F of the films on quartz glass agrees with the SPV results which indicated the *n*-type conductivity of $BaZrS_3$. The value of E_{CBM}-E_F = 1.01 eV for films on glassy carbon indicates a midgap position of the Fermi level, although the negative SPV sign still indicates an *n*-type conductivity. This can be explained by a larger surface bandgap compared to that of the bulk found from optical measurements.

The OPTP-derived photoconductivity transients for the $BaZrS_3$ films are shown in Fig. 6. The transient can be described by a double-exponential fit with a fast decay time of 6 ps followed by a longer decay time of about 90 ps. These 2 decay times may arise from a fast trapping of free charge carriers into defects, followed by recombination. The estimated recombination lifetime of < 0.1 ns indicates significant non-radiative recombination, which would have to be reduced by defect engineering and general improvement of material quality for device applications.

The sum mobility of electrons and holes, μ_{n+p}, is obtained from the initial amplitude of the optical-pump–terahertz-probe spectroscopy measurements, yielding values of 2.4 $cm^2V^{-1}s^{-1}$ which is comparable to the value of 2.1 $cm^2V^{-1}s^{-1}$ previously obtained by the same method for $BaZrS_3$ sulfurized from PLD-deposited precursors [9].

4. Conclusion

In conclusion, $BaZrS_3$ thin films were prepared by H_2S sulfurization of solution-processed precursors deposited by spin-coating of an ink consisting of a mixture of iodide and acetate compounds. We show that the addition of a small amount of the halide compound BaI_2 to the solution of acetate compounds leads to an essential improvement of the uniformity of the films and substrate coverage. The morphology, atomic ratio, crystal structure and optoelectronic properties of the $BaZrS_3$ films

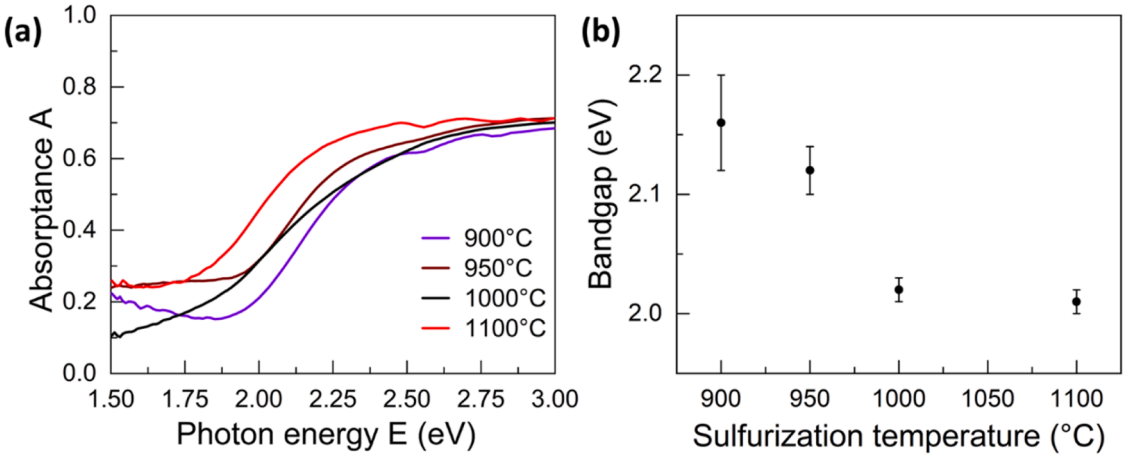

Fig. 4. a) Absorptance of the films sulfurized at 900 °C (violet), 950 °C (brown), 1000 °C (black) and 1100 °C (red). b) Bandgap comparison of the $BaZrS_3$ samples produced by solution process at various sulfurization temperatures.

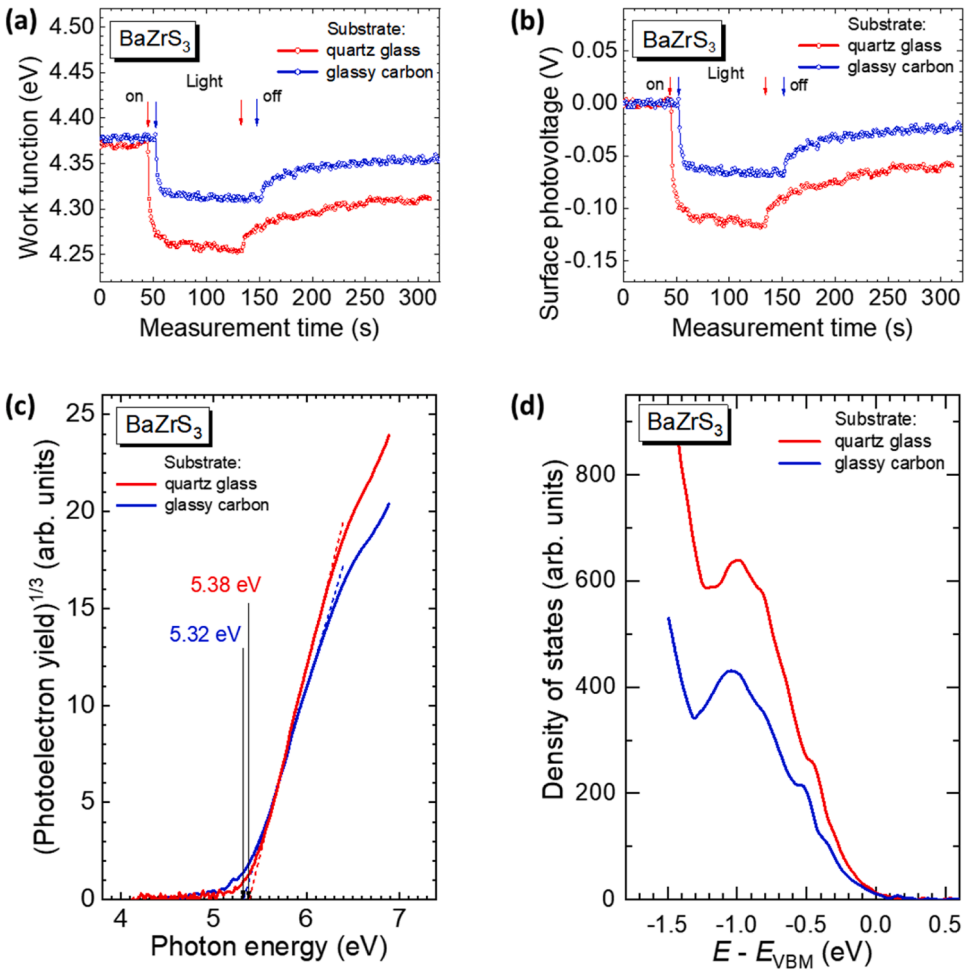

Fig. 5. Electronic properties of $BaZrS_3$ thin films sulfurized at 1000 °C on quartz glass and glassy carbon substrates: (a) Work Function, (b) Surface Photovoltage, (c) Photoelectron Yield spectra with the determined values of ionization energies, and (d) total density of states spectra with the energy scale indicated with respect to the valence band maximum energy E_{VBM}.

Table 2
Summary of the experimental values with error from the optoelectronic measurements.

Sample	CPD (mV) (±2 mV)		SPV (mV) (±3 mV)	Φ (eV) (±0.04 eV)		E_i (eV) (±0.03 eV)	E_F - E_{VBM} (eV) (±0.05 eV)		Bandgap (eV)	μ_{n+p} ($cm^2V^{-1}s^{-1}$)
	Dark	Light		Dark	Light		Dark	Light		
$BaZrS_3$ @1000 °C	−263	−329	−66	4.38	4.31	5.32	−0.94	−1.01	2.02	2.4

were investigated as a function of sulfurization temperature of precursor layers between 600–1100 °C. SEM showed that the crystallite size increased in correlation with the increase in sulfurization temperature, reaching ≈1 μm. The XRF measurements showed that [Ba]/[Zr] ratios of ≈1/1 were not influenced by the sulfurization temperature. Considering the charge neutrality for the films of 1:1:3 stoichiometry, we concluded that no significant amounts of secondary phases are present in the thin films prepared at 1000 °C. The XRD pattern showed prominent peaks of the orthorhombic perovskite crystal structure of $BaZrS_3$ (space group *Pnma, #62*). The best crystallinity and absence of secondary phases showed the films sulfurized at 1000 °C. At 1100 °C a small amount of secondary Ruddlesden-Popper phase of $Ba_4Zr_3S_{10}$ was observed. The bandgap of the single phase $BaZrS_3$ films prepared at 1000 °C was found of 2.02 eV. Kelvin probe measurements demonstrated that these films are of an *n*-type conductivity with a work function of 4.26 eV. Photoelectron yield spectroscopy revealed an ionization energy of 5.38 eV, which defines the position of the valence band maximum. The experimental DOS spectra are found in good agreement with the theoretical data. The charge carrier sum mobility, determined from optical-pump–terahertz-probe spectroscopy measurements, amounts to ≈2.4 $cm^2V^{-1}s^{-1}$ which is comparable to previously published data on H_2S sulfurized $BaZrS_3$ thin films.

This study demonstrates the preparation of $BaZrS_3$ thin films from solution-processed precursors, avoiding the formation of secondary phases. A stoichiometric 1:1:3 atomic ratio was identified as a critical parameter for achieving a high degree of sulfurization with minimal oxygen impurities. Although the annealing temperature remains elevated for industrial applications, the results show that solution-processed precursors can be sulfurized to a high degree, and samples produced at temperatures below 1000 °C also exhibit considerably high sulfurization rates. Extending the sulfurization duration or increasing the H_2S concentration in the argon atmosphere may further improve the sulfurization degree at lower annealing temperatures.

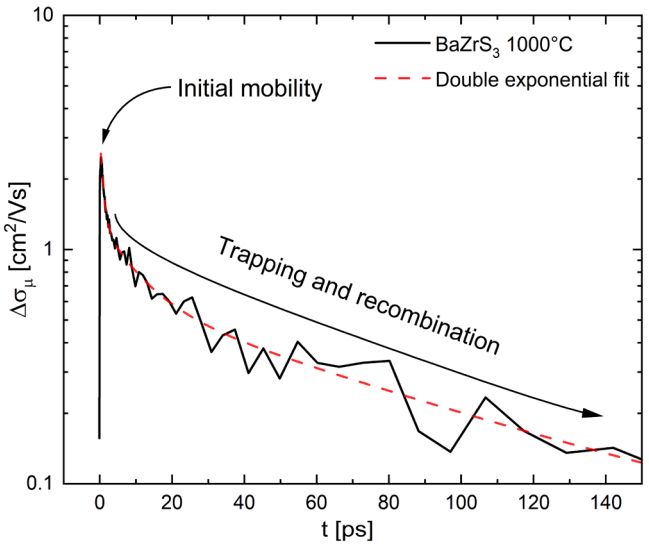

Fig. 6. Photoconductivity transient of ink-based $BaZrS_3$ from the optical-pump-probe spectroscopy and the corresponding double-exponential fit.

CRediT authorship contribution statement

Ibrahim Simsek: Writing – original draft, Visualization, Investigation, Formal analysis, Data curation, Conceptualization. **Marin Rusu:** Writing – review & editing, Conceptualization. **Galina Gurieva:** Formal analysis. **Hannes Hempel:** Formal analysis. **Adriana Röttger:** Formal analysis, Data curation. **José A. Márquez:** Formal analysis. **Thomas Unold:** Supervision, Project administration. **Susan Schorr:** Project administration, Funding acquisition, Formal analysis.

Declaration of competing interest

The authors declare that they have no known competing financial interests or personal relationships that could have appeared to influence the work reported in this paper.

Acknowledgements

We acknowledge Lars Steinkopf for his support to prepare the quartz substrates. Rene Schwiddessen is acknowledged for the XRD measurements. Ibrahim Simsek acknowledges the financial support of the Ministry of National Education of the Republic of Turkey gratefully.

Appendix

Spin-coated $BaZrS_3$ thin films prepared by using only barium iodide as barium source show a good coverage as it can be seen in Fig. A1**(a)**, while using only barium acetate as barium source resulted in an uneven coverage due to agglomeration and possibly dissolved layer when another cycle of spin-coating was performed (see Fig. A1**(b)**).

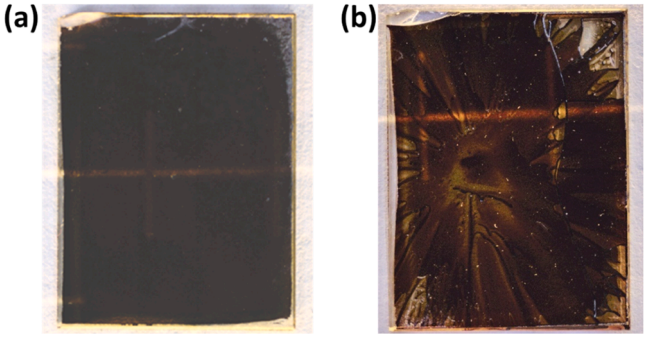

Fig. A1. Optical images of the sulfurized $BaZrS_3$ thin films prepared by using a) only barium iodide as a barium source and b) only acetate compounds.

However, sulfurization of only iodide binaries at 1000 °C resulted in $BaZrS_3$ films which comprised a secondary phase of zirconium (IV) oxide (**see** Fig. A2**(a)**), which did not incorporate the perovskite structure in the required temperature range. This is explained by the different sulfurization kinetics of barium iodide and zirconium (IV) iodide in the investigated temperature range.

Yet using only the acetate compounds did not result in good coverage on the substrate. Most of the material slipped away off the substrate and the still remaining material was washed away during the following spin-coating cycles, which were needed for reaching the desired film thickness. This development can be seen as an intensive X-ray diffraction (XRD) peak in Fig. A2**(a)** which corresponds to the bigger crystalline domain size in Fig. A2 **(b)**.

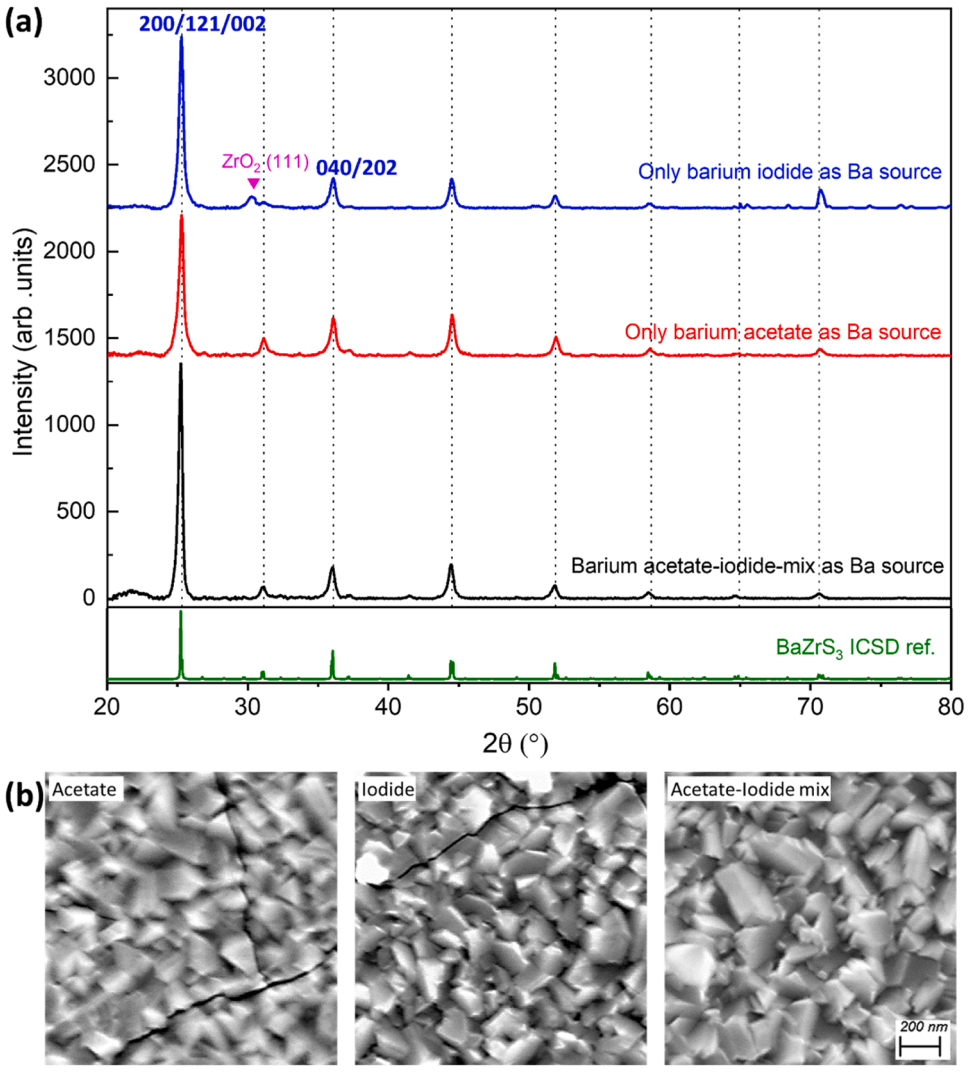

Fig. A2. a) Comparison of the XRD patterns of the $BaZrS_3$ thin films which use different barium compounds: Barium iodide (blue), barium acetate (red), mixture of barium acetate and barium iodide (black) and the ICSD references of ZrO_2 (magenta, ICSD-41011) and $BaZrS_3$ (green, ICSD-23288). b) SEM images of the $BaZrS_3$ thin films which use different barium compounds. The scale applies to all the SEM images.

Le Bail analyses of GIXRD data were done for the samples measured with different incidence angles to identify the phases present in the films. The $Ba_4Zr_3S_{10}$ phase was identified in the film sulfurized at 1100 °C (see Fig. A3), whereas the same phase was not observed in the film sulfurized at 1000 °C (see Fig. A4).

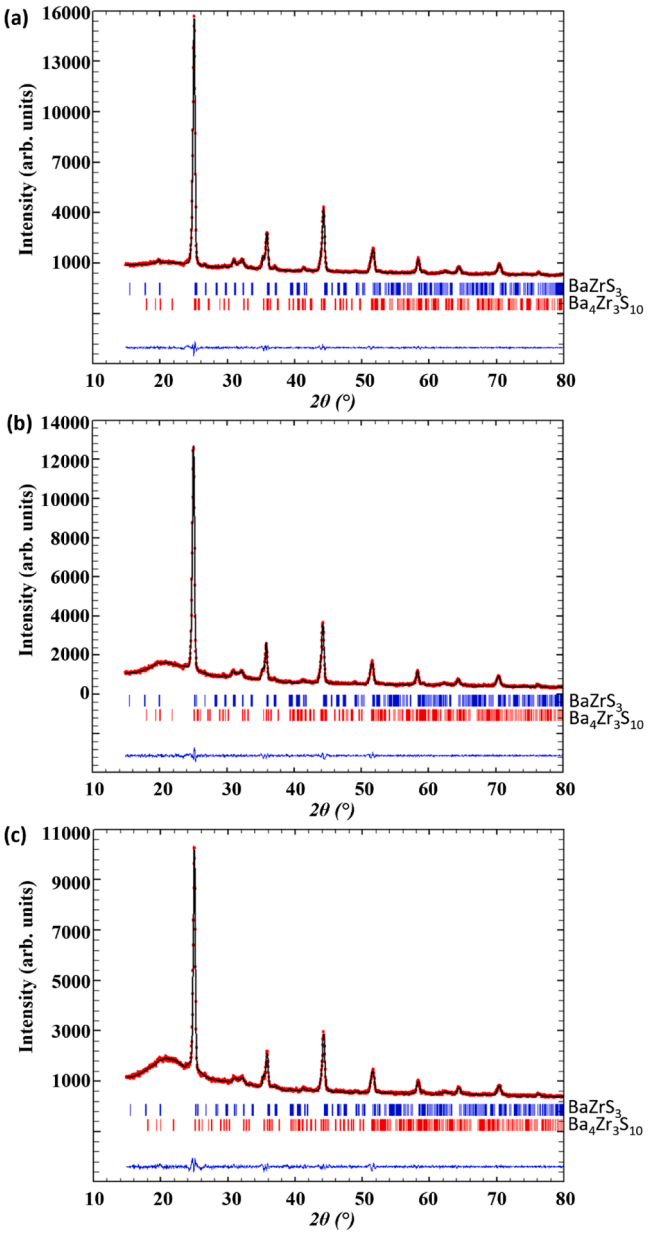

Fig. A3. Grazing incidence XRD patterns of the $BaZrS_3$ sample sulfurized at 1100 °C. a-c) The incident beams were set at angles of 0.5, 1 and 1.5°, respectively. The solid black line is the Le Bail fit of the experimental data (red dots) including an orthorhombic $BaZrS_3$ phase and a cubic $Ba_4Zr_3S_{10}$ phase in the refinement. The blue and red bars represent the Bragg peak positions of $BaZrS_3$ and $Ba_4Zr_3S_{10}$, respectively.

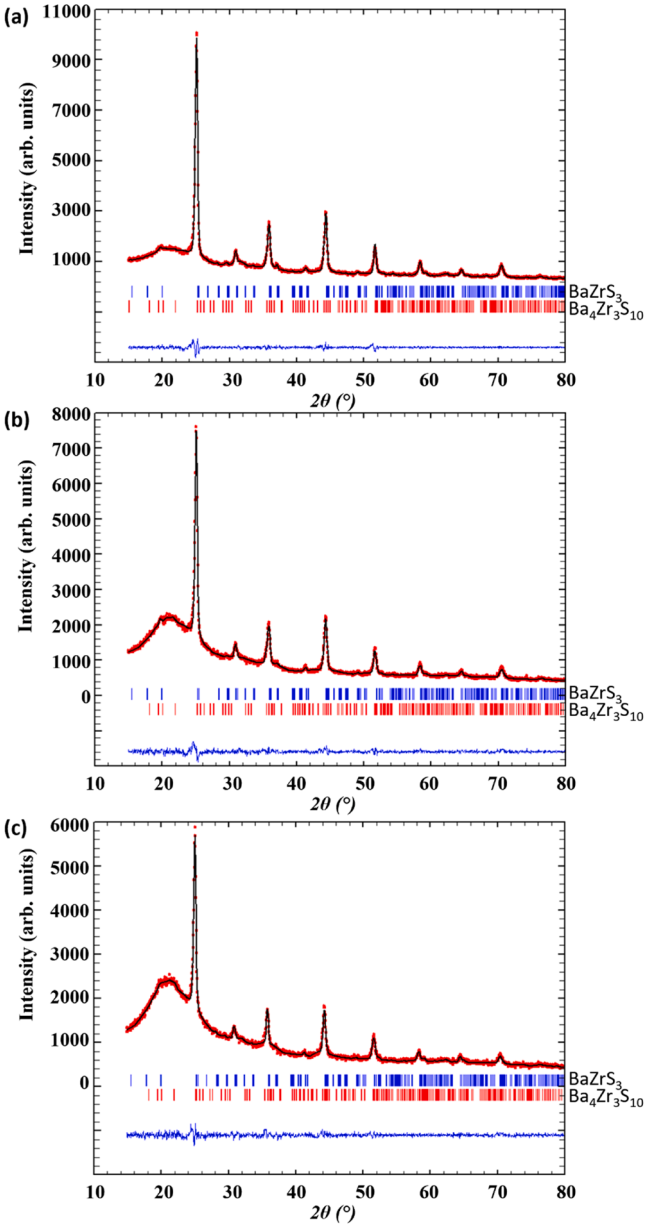

Fig. A4. Grazing incidence XRD patterns of the $BaZrS_3$ sample sulfurized at 1000 °C. a-c) The incident beams were set at angles of 0.5, 1 and 1.5°, respectively. The solid black line is the Le Bail fit of the experimental data (red dots) including an orthorhombic $BaZrS_3$ phase. The blue and red bars represent the Bragg peak positions of $BaZrS_3$ and $Ba_4Zr_3S_{10}$, respectively.

For $BaZrS_3$, the 121 Bragg peak is the strongest one as can be seen in Fig. A2**(a)**. Close to the 121 peak, 200 and 002 Bragg peaks occur as well. Those peaks cannot be resolved since they are too close to each other. In case of statistical orientation of $BaZrS_3$ grains, the similarity between the powder reference and the solution-deposited films in the dominance of the 200/121/002 reflections suggests that the solution process yields a near-random orientation distribution or preserves the bulk texture, whereas the enhanced 040/202 peaks in PLD samples point to directional growth kinetics [9]. Our films do not have a preferred orientation on any of the sulfurization temperatures. The full width at half maximum (FWHM) values of the Bragg peaks give information about the crystallinity of the material. As can be seen in Fig. A5, the crystallinity of the films increases as the annealing temperature increases. It does not decrease further for temperatures >1000 °C.

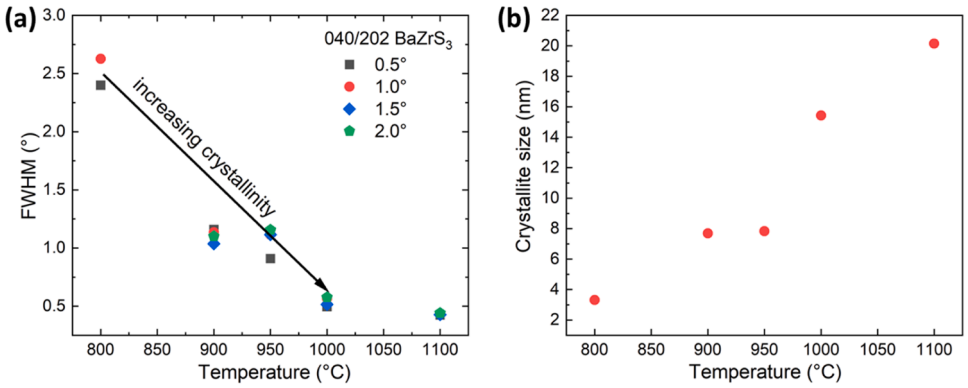

Fig. A5. a) Comparison of the crystallinity of solution-processed $BaZrS_3$ thin films at various sulfurization temperatures by using the full width at half maximums (FWHM) of the 040/202 Bragg peaks. The various colors indicate the samples measured by GIXRD at different grazing incidence angles. b) Crystallite sizes for each sulfurization temperature at their measured GIXRD at the incidence angle of 1°.

To estimate the bandgap, the first derivative of the absorptance is calculated as can be seen in Fig. A6. The details of the calculation are explained in our previous work.

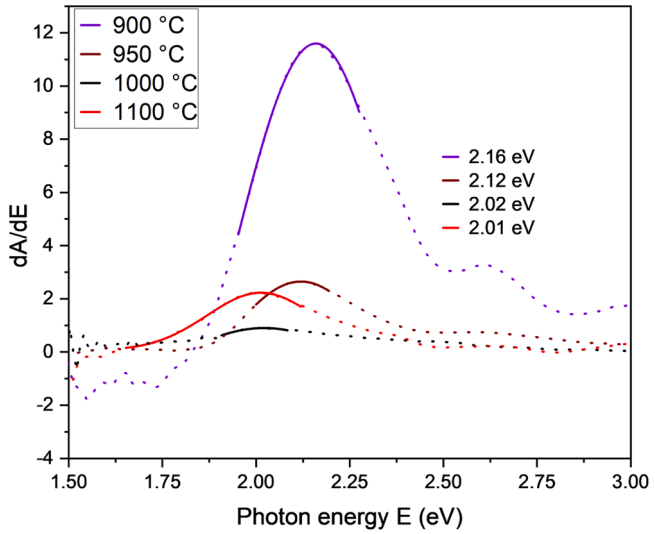

Fig. A6. The derivative of the absorptance (dotted) and their Gaussian fits (line) are used for the determination of the bandgap energy values of the films. The maxima of the fits estimate the bandgaps, and the dots represent the measurement steps.

Data availability

Data will be made available on request.

References

[1] A. Al-Ashouri, E. Köhnen, B. Li, A. Magomedov, H. Hempel, P. Caprioglio, J. A. Márquez, A.B. Morales Vilches, E. Kasparavicius, J.A. Smith, N. Phung, D. Menzel, M. Grischek, L. Kegelmann, D. Skroblin, C. Gollwitzer, T. Malinauskas, M. Jošt, G. Matič, B. Rech, R. Schlatmann, M. Topič, L. Korte, A. Abate, B. Stannowski, D. Neher, M. Stolterfoht, T. Unold, V. Getautis, S. Albrecht, Monolithic perovskite/silicon tandem solar cell with >29% efficiency by enhanced hole extraction, Science 370 (2020) 1300–1309, https://doi.org/10.1126/science.abd4016.

[2] Best Research-Cell Efficiency Chart, (n.d.). https://www.nrel.gov/pv/cell-efficiency.html.

[3] Y.-Y. Sun, M.L. Agiorgousis, P. Zhang, S. Zhang, Chalcogenide perovskites for photovoltaics, Nano Lett. 15 (2015) 581–585, https://doi.org/10.1021/nl504046x.

[4] S. Perera, H. Hui, C. Zhao, H. Xue, F. Sun, C. Deng, N. Gross, C. Milleville, X. Xu, D. F. Watson, B. Weinstein, Y.-Y. Sun, S. Zhang, H. Zeng, Chalcogenide perovskites – an emerging class of ionic semiconductors, Nano Energy 22 (2016) 129–135, https://doi.org/10.1016/j.nanoen.2016.02.020.

[5] M.-G. Ju, J. Dai, L. Ma, X.C. Zeng, Perovskite chalcogenides with optimal bandgap and desired optical absorption for photovoltaic devices, Adv. Energy Mater. 7 (2017) 1700216, https://doi.org/10.1002/aenm.201700216.

[6] S.A. Filippone, Y.-Y. Sun, R. Jaramillo, Determination of adsorption-controlled growth windows of chalcogenide perovskites, MRC 8 (2018) 145–151, https://doi.org/10.1557/mrc.2018.10.

[7] T. Gupta, D. Ghoshal, A. Yoshimura, S. Basu, P.K. Chow, A.S. Lakhnot, J. Pandey, J. M. Warrender, H. Efstathiadis, A. Soni, E. Osei-Agyemang, G. Balasubramanian, S. Zhang, S. Shi, T. Lu, V. Meunier, N. Koratkar, An environmentally stable and lead-free chalcogenide perovskite, Adv. Funct. Mater. (2020) 2001387, https://doi.org/10.1002/adfm.202001387.

[8] X. Wei, H. Hui, C. Zhao, C. Deng, M. Han, Z. Yu, A. Sheng, P. Roy, A. Chen, J. Lin, D.F. Watson, Y.-Y. Sun, T. Thomay, S. Yang, Q. Jia, S. Zhang, H. Zeng, Realization of $BaZrS_3$ chalcogenide perovskite thin films for optoelectronics, Nano Energy 68 (2020) 104317, https://doi.org/10.1016/j.nanoen.2019.104317.

[9] J.A. Márquez, M. Rusu, H. Hempel, I.Y. Ahmet, M. Kölbach, I. Simsek, L. Choubrac, G. Gurieva, R. Gunder, S. Schorr, T. Unold, $BaZrS_3$ chalcogenide perovskite thin films by H_2S sulfurization of oxide precursors, J. Phys. Chem. Lett. 12 (2021) 2148–2153, https://doi.org/10.1021/acs.jpclett.1c00177.

[10] C. Comparotto, A. Davydova, T. Ericson, L. Riekehr, M.V. Moro, T. Kubart, J. Scragg, Chalcogenide perovskite $BaZrS_3$: thin film growth by sputtering and rapid thermal processing, ACS Appl. Energy Mater. 3 (2020) 2762–2770, https://doi.org/10.1021/acsaem.9b02428.

[11] I. Sadeghi, K. Ye, M. Xu, Y. Li, J.M. LeBeau, R. Jaramillo, Making $BaZrS_3$ chalcogenide perovskite thin films by Molecular Beam epitaxy, Adv. Funct. Mater. 31 (2021) 2105563, https://doi.org/10.1002/adfm.202105563.

[12] K. Ye, I. Sadeghi, M. Xu, J. Van Sambeek, T. Cai, J. Dong, R. Kothari, J.M. LeBeau, R. Jaramillo, A processing route to chalcogenide perovskites alloys with tunable band gap via Anion Exchange, Adv. Funct. Mater. (2024) 2405135, https://doi.org/10.1002/adfm.202405135.

[13] W. Meng, B. Saparov, F. Hong, J. Wang, D.B. Mitzi, Y. Yan, Alloying and defect control within chalcogenide perovskites for optimized photovoltaic application, Chem. Mater. 28 (2016) 821–829, https://doi.org/10.1021/acs.chemmater.5b04213.
[14] S. Agarwal, K.C. Vincent, J.W. Turnley, D.C. Hayes, M.C. Uible, I. Durán, A.S. M. Canizales, S. Khandelwal, I. Panicker, Z. Andoh, R.M. Spilker, Q. Ma, L. Huang, S. Hwang, K. Kisslinger, S. Svatek, E. Antolin, S.C. Bart, R. Agrawal, Breaking barriers in chalcogenide perovskite synthesis: a generalized framework for fabrication of BaMS3 (M=Ti, Zr, Hf) materials, Adv. Funct. Mater. 34 (2024) 2405416, https://doi.org/10.1002/adfm.202405416.
[15] X. Wei, H. Hui, S. Perera, A. Sheng, D.F. Watson, Y.-Y. Sun, Q. Jia, S. Zhang, H. Zeng, Ti-alloying of $BaZrS_3$ chalcogenide perovskite for photovoltaics, ACS Omega 5 (2020) 18579–18583, https://doi.org/10.1021/acsomega.0c00740.
[16] S. Sharma, Z. Ward, K. Bhimani, K. Li, A. Lakhnot, R. Jain, S.-F. Shi, H. Terrones, N. Koratkar, Bandgap tuning in $BaZrS_3$ perovskite thin films, ACS Appl. Electron. Mater. (2021) acsaelm.1c00575, https://doi.org/10.1021/acsaelm.1c00575.
[17] W.G. Van Der Sluys, The solubility rules: why are all acetates soluble? J. Chem. Educ. 78 (2001) 111, https://doi.org/10.1021/ed078p111.
[18] J. Sarfraz, A. Määttänen, P. Ihalainen, M. Keppeler, M. Lindén, J. Peltonen, Printed copper acetate based H_2S sensor on paper substrate, Sens. Actuators B: Chem. 173 (2012) 868–873, https://doi.org/10.1016/j.snb.2012.08.008.
[19] A.W. Davidson, Solutions of salts in pure acetic acid. I. Preliminary paper, J. Am. Chem. Soc. 50 (1928) 1890–1895, https://doi.org/10.1021/ja01394a009.
[20] Y. Wang, N. Sato, K. Yamada, T. Fujino, Synthesis of $BaZrS_3$ in the presence of excess sulfur, J. Alloys Compd. 311 (2000) 214–223, https://doi.org/10.1016/S0925-8388(00)01134-8.
[21] Y. Wang, N. Sato, T. Fujino, Synthesis of $BaZrS_3$ by short time reaction at lower temperatures, J. Alloys Compd. 327 (2001) 104–112, https://doi.org/10.1016/S0925-8388(01)01553-5.
[22] M. Rusu, T. Kodalle, L. Choubrac, N. Barreau, C.A. Kaufmann, R. Schlatmann, T. Unold, Electronic structure of the CdS/Cu(In,Ga)Se_2 interface of KF- and RbF-treated samples by Kelvin probe and photoelectron yield spectroscopy, ACS Appl. Mater. Interfaces 13 (2021) 7745–7755, https://doi.org/10.1021/acsami.0c20976.
[23] H. Hempel, A. Redinger, I. Repins, C. Moisan, G. Larramona, G. Dennler, M. Handwerg, S.F. Fischer, R. Eichberger, T. Unold, Intragrain charge transport in kesterite thin films—limits arising from carrier localization, J. Appl. Phys. 120 (2016) 175302, https://doi.org/10.1063/1.4965868.
[24] A. Röttger, M. Rusu, H. Hempel, Á.L. Álvarez, M. Dimitrievska, D. Abou-Ras, I. Simsek, R. Schwiddessen, S. Schorr, T. Unold, Effect of composition on structural and optoelectronic properties of combinatorial $BaZrS_3$ thin films, [Preprint], ChemRxiv (2026), https://doi.org/10.26434/chemrxiv.15002184/v1.
[25] D. Pareek, T. Taskesen, J.A. Márquez, H. Stange, S. Levcenco, I. Simsek, D. Nowak, T. Pfeiffelmann, W. Chen, C. Stroth, M.H. Sayed, U. Mikolajczak, J. Parisi, T. Unold, R. Mainz, L. Gütay, Reaction pathway for efficient $Cu_2ZnSnSe_4$ solar cells from alloyed Cu-Sn precursor via a Cu-rich selenization stage, Sol. RRL 4 (2020) 2000124, https://doi.org/10.1002/solr.202000124.
[26] S. Niu, D. Sarkar, K. Williams, Y. Zhou, Y. Li, E. Bianco, H. Huyan, S.B. Cronin, M. E. McConney, R. Haiges, R. Jaramillo, D.J. Singh, W.A. Tisdale, R. Kapadia, J. Ravichandran, Optimal bandgap in a 2D Ruddlesden–Popper perovskite chalcogenide for single-junction solar cells, Chem. Mater. 30 (2018) 4882–4886, https://doi.org/10.1021/acs.chemmater.8b01707.
[27] W. Li, S. Niu, B. Zhao, R. Haiges, Z. Zhang, J. Ravichandran, A. Janotti, Band gap evolution in Ruddlesden-Popper phases, Phys. Rev. Mater. 3 (2019) 101601, https://doi.org/10.1103/PhysRevMaterials.3.101601.
[28] S. Niu, Perovskite Chalcogenides: Emerging Semiconductors for Visible to Infrared, Dissertation, University of Southern California, 2019. https://www.proquest.com/openview/d0a052641e3d4abc4a1363b0171b6e0c/1?pq-origsite=gscholar&cbl=18750&diss=y.
[29] S. Niu, B. Zhao, K. Ye, E. Bianco, J. Zhou, M.E. McConney, C. Settens, R. Haiges, R. Jaramillo, J. Ravichandran, Crystal growth and structural analysis of perovskite chalcogenide $BaZrS_3$ and ruddlesden-popper phase $Ba_3Z_2S_7$, J. Mater. Res. 34 (2019) 3819–3826, https://doi.org/10.1557/jmr.2019.348.
[30] A.A. Pradhan, S. Agarwal, K.C. Vincent, D.C. Hayes, J.M. Peterson, J.W. Turnley, R. M. Spilker, M.C. Uible, S.C. Bart, L. Huang, K. Kisslinger, R. Agrawal, Emergence of Ruddlesden–Popper phases and other pitfalls for moderate temperature solution deposited chalcogenide perovskites, Mater. Chem. Front. (2024) 3358–3372, https://doi.org/10.1039/D4QM00441H.
[31] P. Kayastha, D. Tiwari, A. Holland, O.S. Hutter, K. Durose, L.D. Whalley, G. Longo, High-temperature equilibrium of 3D and 2D chalcogenide perovskites, Sol. RRL 7 (2023) 2201078, https://doi.org/10.1002/solr.202201078.
[32] E. Osei-Agyemang, N. Koratkar, G. Balasubramanian, Examining the electron transport in chalcogenide perovskite $BaZrS_3$, J. Mater. Chem. C 9 (2021) 3892–3900, https://doi.org/10.1039/D1TC00374G.